



HAL
open science

Minimal architecture lithium batteries: toward high energy density storage solutions

Jacopo Celè, Sylvain Franger, Yann Lamy, Sami Oukassi

► **To cite this version:**

Jacopo Celè, Sylvain Franger, Yann Lamy, Sami Oukassi. Minimal architecture lithium batteries: toward high energy density storage solutions. *Small*, 2023, 2023, pp.2207657. 10.1002/sml.202207657 . hal-04072100

HAL Id: hal-04072100

<https://hal.science/hal-04072100>

Submitted on 17 Apr 2023

HAL is a multi-disciplinary open access archive for the deposit and dissemination of scientific research documents, whether they are published or not. The documents may come from teaching and research institutions in France or abroad, or from public or private research centers.

L'archive ouverte pluridisciplinaire **HAL**, est destinée au dépôt et à la diffusion de documents scientifiques de niveau recherche, publiés ou non, émanant des établissements d'enseignement et de recherche français ou étrangers, des laboratoires publics ou privés.



Distributed under a Creative Commons Attribution 4.0 International License

Minimal Architecture Lithium Batteries: Toward High Energy Density Storage Solutions

Jacopo Celè,* Sylvain Franger, Yann Lamy, and Sami Oukassi*

The coupling of thick and dense cathodes with anode-free lithium metal configuration is a promising path to enable the next generation of high energy density solid-state batteries. In this work, LiCoO_2 (30 μm)/LiPON/Ti is considered as a model system to study the correlation between fundamental electrode properties and cell electrochemical performance, and a physical model is proposed to understand the governing phenomena. The first cycle loss is demonstrated to be constant and independent of both cathode thickness and anode configuration, and only ascribed to the diffusion coefficient's abrupt fall at high lithium contents. Subsequent cycles achieve close to 100% coulombic efficiency. The examination of the effect of cathode thickness demonstrate a nearly linear correlation with areal specific capacity for sub-100 μm LiCoO_2 and 0.1 mA cm^{-2} current density. These findings bring new insights to better understand the energy density limiting factors and to suggest potential optimization approaches.

strategies have been applied for cathode optimization, including materials selection and architecture design.^[6,7] In the framework of higher energy density, the increase in cathode thickness in a composite electrode structure has been the most common approach.^[8,9] This design exploits the theory of porous electrode in order to decrease the internal resistance inside the cathode.^[10–12] More recently, thick and dense all-electrochemically-active cathodes with controlled orientation and continuous architecture have been considered as one of the most promising options for the next battery generation.^[13–16] This configuration pushes the cathode capacity to its theoretical limits, by elimination of binders and other additives. Moreover, it ensures, in the case of monolithic cathode, the suppression of

grains boundary, which has been shown to be the main limitation in solid state composite electrode.^[16,17] Additionally, the lithium metal has been considered to be the best solution for decades, but in the last years the anode-free solution gained in popularity. In fact, the lithium the cathode can intercalate is already present in the active material itself, that is to say, the lithium which is actually used during the charge/discharge process is only the lithium inside the active material and not the lithium of the anode layer. The latter acts only as a substrate for the plating and stripping of the native lithium, and is used to compensate any loss of lithium element due to irreversible reactions. By suppressing this lithium layer, anode-free cells achieve unrivalled energy density.^[18–20] Notwithstanding, the absence of any lithium backup to compensate for irreversible loss is also a risk factor. In particular, the anode free technology suffers from a poor cycling performance when compared to the lithium-metal counterpart.^[19] Two main mechanisms are responsible for the poor cyclability: irreversible reaction during the creation of the solid-electrolyte interface (SEI) and the formation of voids during the stripping/plating process of lithium.^[18,21,22] In the present work, we won't address the long term cyclability.

To the best of our knowledge, combining both anode-free and all-electrochemically-active cathode, in one single solid-state battery, has not been reported in literature. In this work, we propose a model system using transition metal dioxide, typified by LiCoO_2 (LCO),^[23] a solid inorganic glass LiPON electrolyte and a titanium current collector to study the correlation between intrinsic electrodes properties and cell electrochemical performance. We also develop a physical model to understand the governing phenomena based on weak form partial

1. Introduction

The development of high energy density solid state batteries (SSBs) is critical to meet the ever-growing energy demand for a wide range of applications.^[1,2] Both consumer electronics and electric vehicles (EV) producers crave for the deployment of this new technology, as a key factor to dominate the upcoming markets.^[3–5] SSBs present distinctive features compared to the liquid counterpart, namely improved safety, higher energy density, lower self-discharge and higher cycle life. Up to now, altogether with a focus on high conductive electrolyte, researchers' efforts have focused on the increasing of energy per volume at the positive and negative electrodes in order to make SSBs affordable and competitive for targeted applications. Multiple

J. Celè, Y. Lamy, S. Oukassi
Univ. Grenoble Alpes, CEA, Leti
Grenoble F-38000, France
E-mail: jacopo.cele@cea.fr; sami.oukassi@cea.fr

J. Celè, S. Franger
ICMMO (UMR CNRS 8182)
Univ. Paris-Sud
Univ. Paris-Saclay
Orsay 91190, France

 The ORCID identification number(s) for the author(s) of this article can be found under <https://doi.org/10.1002/smll.202207657>.

© 2023 The Authors. Small published by Wiley-VCH GmbH. This is an open access article under the terms of the Creative Commons Attribution License, which permits use, distribution and reproduction in any medium, provided the original work is properly cited.

DOI: 10.1002/smll.202207657

differential equations (PDE) for lithium drift and diffusion, implemented and solved in COMSOL Multiphysics. The model is developed starting from a 1D drift/diffusion model for solid-state batteries.^[24–27] Implementation details are reported in the dedicated section. The anode-free configuration is validated as an alternative to lithium metal, and the cyclability of the full-stack is demonstrated. The maximum discharge capacity achieved reaches 1.2 mA h cm⁻², the highest reported for a 30 μm thick cathode in a solid state anode-free device. By coupling anode-free with 100% active cathode, the cells can achieve the stunning volumetric capacity of 1400 W h L⁻¹. Multiple cathode thickness devices are reported, and the physical model is validated experimentally up to 30 μm thick LCO, showing a linear correlation between cathode thickness and delivered capacity for current densities up to 2 mA cm⁻². Furthermore, electrochemical performance are analyzed from a physical point of view and the ability of monolithic LCO to sustain high current density, without major capacity loss, is demonstrated. The developed model has been used to explain the first-cycle loss in LCO, showing the capacity loss proportionality with the cathode thickness and the link with the semiconductor-to-metal transition of LCO at high intercalation fraction. Diffusion limitation appears for states of charge (SOC) below 50%. As long as the battery charge is >50%, no limitation comes from the cathode and thicker electrode design is even beneficial, with a total available capacity increasing with thickness. In the concluding sections, we present prospective results for cathode thickness up to 100 μm, which are the highest proposed so far.^[16,28] Moreover, starting from the insight on the interface accumulation obtained by means of physical simulation, we review the main strategy reported in literature to suppress it. Our results can be extended to other cell configurations: for example, to estimate performance of a single particle of given diameter, which serves to tailor optimal grain size and decouple effects related to grain boundaries and binder/additive in composite electrodes. Moreover, control over lithium transport may prove useful to design battery management systems capable of avoiding strong accumulation and completely exploiting the available capacity.

2. Results

2.1. Physical Characterization of the Cell

The device under test (Figure 1a) was realized on a 8'' Si/SiO₂ substrate. The active stack consists in: Pt current collector, LCO cathode, LiPON solid electrolyte, and Ti negative (current) electrode. A polymer encapsulation protects the device from the atmosphere, and a redistribution layer enables the negative electrode polarization. Details about the fabrication are reported elsewhere.^[29] When describing this system by means of 1D equations along deposition direction (x-axis), we are assuming spatial homogeneity on the y-z plane at any x position. Moreover, in the present case, we assume the physical properties to be a function of the lithium concentration only. The model assumption is a homogeneity of the physical properties along the three spatial coordinates. In order to validate this hypothesis, an extensive physical characterization has been

carried out. Once the spatial homogeneity has been proven, the model can be applied to different cell architectures (i.e., LCO thickness), without any modification of the physical parameters. From literature,^[30–32] it is known that, after physical vapour deposition, LCO is present in the (003) crystalline orientation only, corresponding (Figure 1b) to a c axis (c_x) perpendicular to the deposition surface and leading to a slow lithium diffusion.^[32–36] The component of the normalized c vector along x ($c_x = \cos(0)$, $c_x = \cos(\pi)$) is equal to ± 1 . After crystallization at high temperature, the observed preferential orientation is reported to be (101)^[32,36,37] (Figure 1b), which presents the c axis oriented at $\approx 73^\circ$ with respect to the deposition plane, with a c_x component of ± 0.3 . The (101) is a favorable orientation due to the quasi-parallel orientation of the diffusion channels and the film growth axis. Another observable phase is the (104), which presents a 40° angle between the diffusion channels and the deposition plane (Figure 1b), corresponding to a value of c_x around ± 0.6 . Figure 1c depicts a 20 μm thick transmission electron microscopy (TEM) lamella and the corresponding crystalline orientation mapping obtained by precession electron diffraction (PED). In particular, the bottom side refers to the Pt/LCO interface, while the top side refers to the LCO/LiPON. The central zone is the bulk of the electrode. The (003) phase is mapped in light (−451) and dark (+1) yellow. The (101) is mapped with two colors due to a wide distribution: in green between 0.4 and 0.3 and in pink from 0.3 to 0.2. Both (101) and a small residual of the (003) orientation is visible in the histogram reported in Figure 1c for each color. The (101) present a Gaussian-like distribution with a mean value of 0.3. Phase (104), in orange, is present in negligible amount in the sample. Concluding, we can easily compare the three histograms at different cathode film depth, noting that LCO crystalline orientation distribution is almost constant. This is paramount information in order to support the relevance of the measured diffusion coefficient for 5 μm–30 μm cathode thickness. Additional support can be drawn from scanning electron microscopy (SEM) observation and mean deposition rate (Figure 1d). LCO presents a typical columnar structure with few voids. A constant deposition rate is observed, which substantiates a constant LCO density and corroborates the hypothesis of a comparable all-electrochemically-active cathode material within the interval 5–30 μm. By means of Raman spectroscopy, it is possible to delve into the local chemical structure and LCO stoichiometry. Raman spectroscopy is performed on 30 μm thick LCO cross section. The characteristic peak positions A_{1g} (598 cm⁻¹) and E_g (487 cm⁻¹)^[38–40] are mapped in Figure 1f,g. Peak positions are in line with the reported literature for the major part of the analyzed surface. Some isolated spots (in green) present a slight red shift of ≈ 5 cm⁻¹ for both peaks. The shift is accompanied by a minor decrease of the E_g peak intensity, as reported in Figure 1e, where two spectra are presented. These zones should correspond to a slight ($x > 0.95$) delithiation: below this lithium concentration a semiconductor to metal transition is expected, which theoretically corresponds to a strong weakening of the Raman peaks,^[39,41,42] not observed in the present measurement. We consider the difference between the bulk of the observed sample and the localized delithiated zone to be of minor impact, due to almost identical spectra provided by the two species. The shift seems to correlate with local defects of

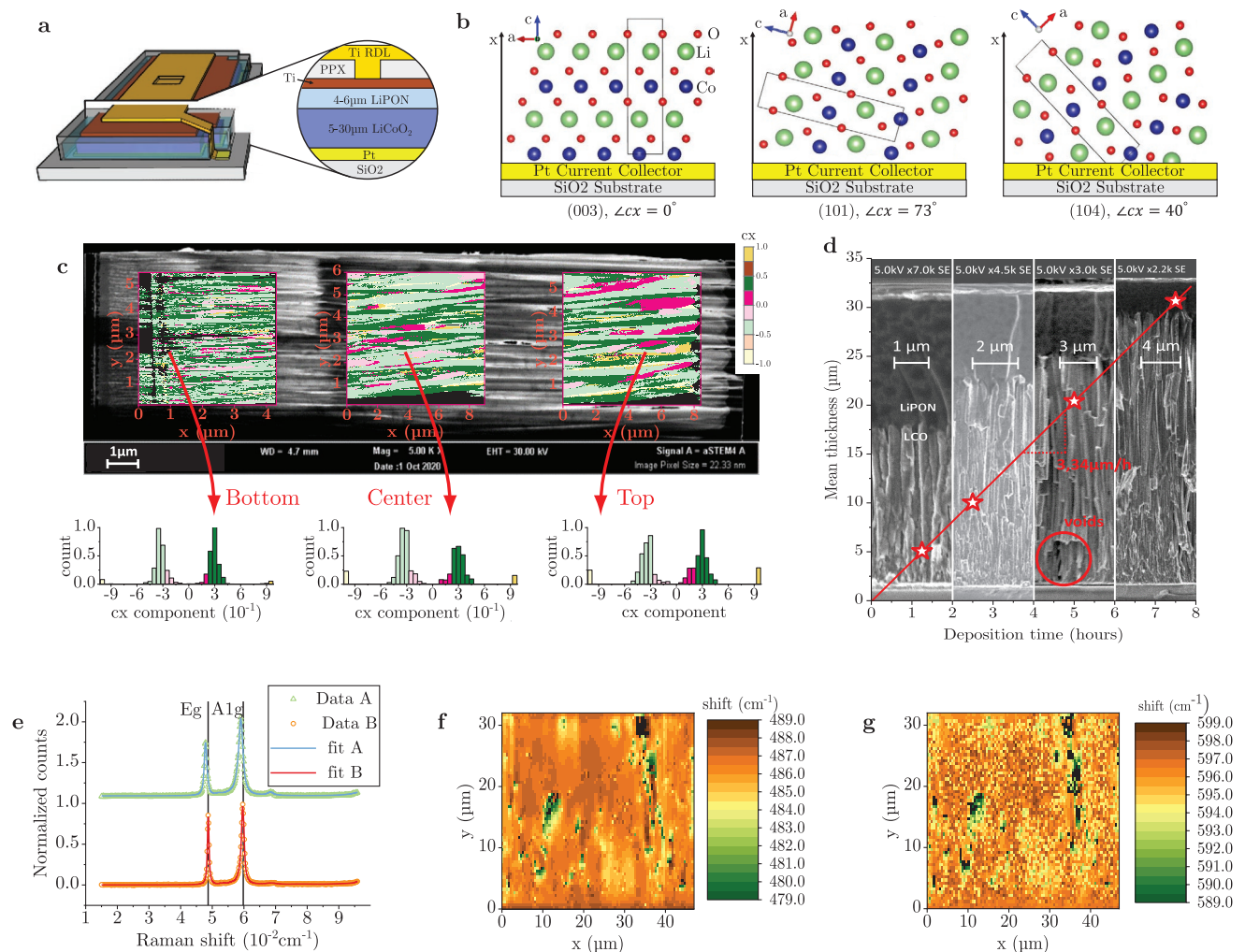


Figure 1. LiCoO₂ spatial homogeneity analysis. a) 3D schematic illustration and cross-sectional view of the device under test. b) Principal crystalline orientations with respect to the PVD deposition substrate; lithium diffusion channel are perpendicular to the c-axis, i.e., high angles correspond to higher diffusion dynamics. c) SEM view of the TEM lamella and crystalline orientations mapping obtained by PED; histograms confirm homogeneous distribution with a predominance of the (101) phase in green between the three acquisition zone: near the deposition substrate (bottom), in the bulk (center), and near the LiPON/LCO interface (top). d) Deposition rate and SEM cross-section of batteries with 5–30 μm LCO cathodes. Linear behavior testifies a constant deposition rate over time for all samples. Black spots correspond to voids in the LCO columnar structure. e) Raman spectra of LCO and 2D mapping of 30 μm LCO cross section for peaks f) Eg and g) A1g.

the LCO structure, likely caused by deposition inhomogeneity (Figure S9, Supporting Information).

2.2. PDE Model Development

Within this context, a 1D path for lithium ions diffusion is considered between the two electrodes as depicted in **Figure 2a**. The axis origin is set at the interface between the positive current collector and the LCO layer. x_{LCO} and x_{LiPON} are the cathode and electrolyte thickness, respectively. c , c_2 and M , M_2 are the normalized lithium concentration inside the two materials and the corresponding mobility, respectively. Assuming the cathode material to be homogeneous, i.e., all parameters depend exclusively on the local concentration of lithium ions

and not on the distance from the origin, we cast the diffusion equation for each domain:

$$\frac{\partial c}{\partial t} = -\frac{1}{\partial x} \left(M c_0 c (1-c) \frac{\partial \tilde{\mu}}{\partial x} \right) \text{ for } 0 < x < x_{LCO} \quad (1)$$

$$\frac{\partial c_2}{\partial t} = -\frac{1}{\partial x} \left(M_2 c_0 c_2 (1-c_2) \frac{\partial \tilde{\mu}_2}{\partial x} \right) \text{ for } x_{LCO} < x < x_{LCO} + x_{LiPON} \quad (2)$$

All constants are listed in **Table 1**. It should be noted here that both equations differ slightly from the standard drift-diffusion equation found in literature.^[43] The LCO model will be discussed in details later, while here we propose to analyze the LiPON related Equation (2). In particular, considering the mathematical amenities that lead to the standard drift-diffusion

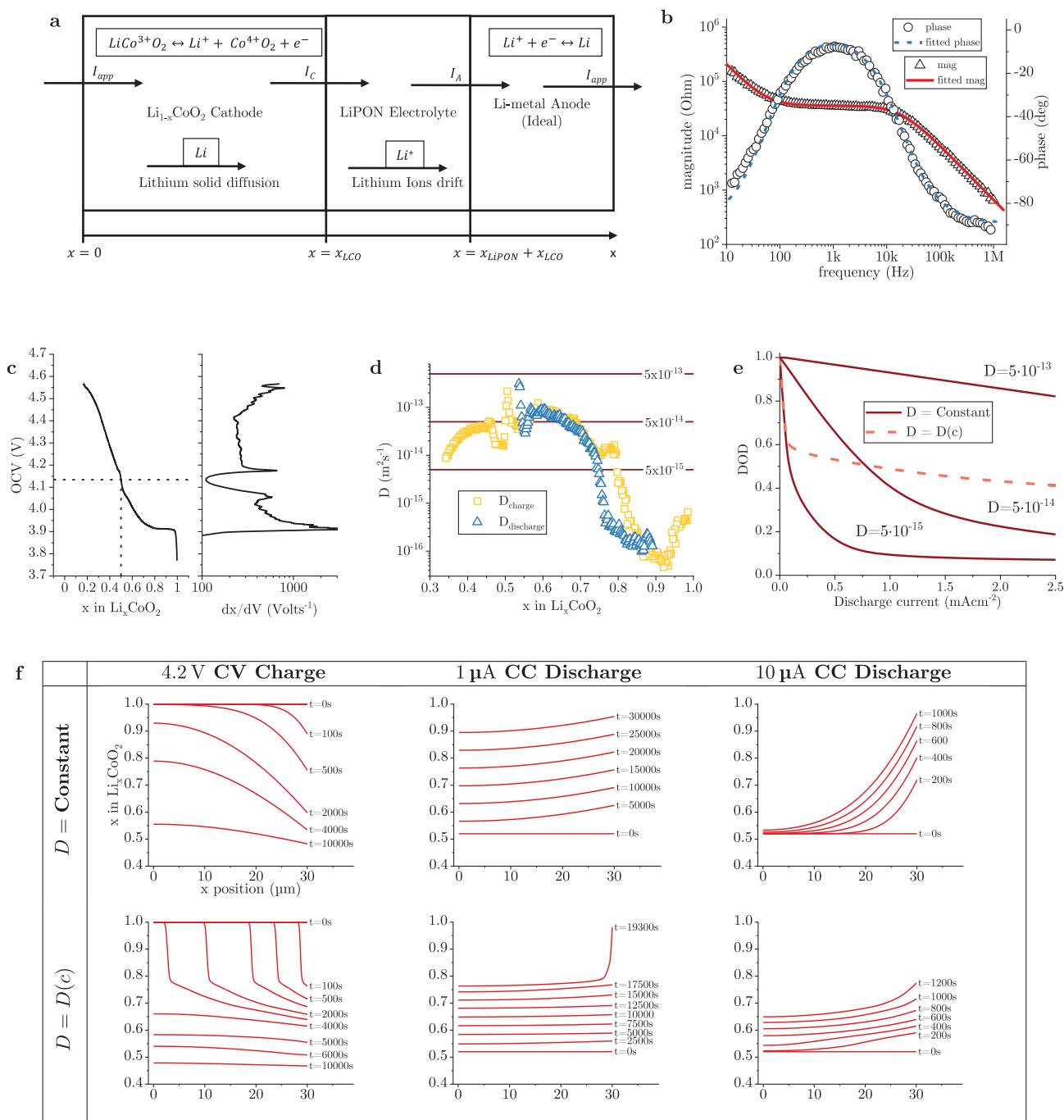


Figure 2. LCO Model development. a) Schematic illustration of the lithium path during charge process in a LCO/LiPON/Li stack. b) Electrochemical impedance spectroscopy measurement and fitting for a Pt/LiPON (4 μm)/Ti structure. c) Measured OCV and its derivative variation with intercalation fraction x (variable c in the model equations); minimum in the derivative correspond to $x = 0.5$ order–disorder transition. d) Diffusion coefficient extracted by mean of GITT for 10 μm thick LCO. e) Comparison of the effect of constant and variable diffusion coefficient on the rate performance of a 30 μm thick LCO thin-film solid state battery, and f) corresponding lithium profile inside LCO for charge and discharge at constant and variable diffusion coefficient: variable diffusion only accounts for sudden lithium accumulation at the interface during discharge.

equation for an electrolyte, we recall the Nernst–Planck flux equation

$$j = -c_2 M_2 \frac{\partial \tilde{\mu}_2}{\partial x} \quad (3)$$

Where M is the mobility and $\tilde{\mu}_2$ the chemical potential of lithium inside LiPON. Usually, for liquid electrolytes, one assumes i) the mobility to be constant with respect to the lithium concentration, ii) the chemical potential to be equal to

Table 1. Model parameters.

Constant	Value	Unit	Description
k_b	$1.38 \cdot 10^{-23}$	J/K	Boltzman constant
T	310.5	K	Temperature
q_0	$1.6 \cdot 10^{-19}$	C	Electron charge
F_c	9.65e4	C/mol	Faraday's constant
ϵ_0	$8.85 \cdot 10^{-12}$	F/m	Vacuum permittivity
ϵ_r	220	1	Lipon dielectric constant
M_{01}	$3.7 \cdot 10^{-14}$	m^2/s	Li mobility in LCO
R_s	10	ohm	Series resistance
A_{elec}	$4.7 \cdot 10^{-7}$	m^2	Electrode surface
c_0	5.6e4	mol/m^3	LCO maximum lithium concentration
α	0.5	1	Symmetry coefficient
R_g	8.314	J/(Kmol)	Gas constant
c_{02}	100	mol/m^3	LiPON maximum lithium concentration
c_{2eq}	50	mol/m^3	LiPON equilibrium lithium concentration
M_{02}	$8.6 \cdot 10^{-11}$	m^2/s	Li mobility in LiPON
i_{01c}	1.17e6	A/m^2	LCO-LiPON cathodic exchange current
i_{02c}	1.17e6	A/m^2	LCO-LiPON anodic exchange current
i_{01a}	1.17e6	A/m^2	Li-LiPON cathodic exchange current
i_{02a}	1.17e6	A/m^2	Li-LiPON anodic exchange current

$$\tilde{\mu}_2 = \mu_{02} + k_b T \ln \gamma c_2 + q_0 \phi \quad (4)$$

With μ_{02} the standard chemical potential, γ the ions activity (equal to unity) and ϕ the electrical potential, we obtain

$$j = -D_2 \frac{\partial c_2}{\partial x} + M_2 q_0 c_2 E \quad (5)$$

Where

$$E = -\frac{\partial \phi}{\partial x} \quad (6)$$

And

$$D = M_2 k_b T \quad (7)$$

In order to obtain the presented equation here, let's reconsider the definition of the chemical potential in Equation (4). This equation was developed for ions transport in liquid electrolyte, where the spatial accumulation of ions is restricted by electrostatic repulsion only. LiPON is not a liquid electrolyte, the transference number of the mobile specie (Li^+) is 1, and the available spatial sites for lithium ions are finite. As a matter of fact, the maximum lithium concentration is bounded. In order to take into account this aspect, the chemical potential and the mobility can be rewritten^[44,45] as:

$$\tilde{\mu}_2 = \mu_{02} + k_b T \ln \gamma \frac{c_2}{1-c_2} + q_0 \phi \quad (8)$$

$$M_2 = M_{02}(1-c_2) \quad (9)$$

For a non-interacting particles system. Inserted back in Equation (3), the LiPON drift-diffusion equation is obtained, as reported in Equation (2). In order to obtain the electrostatic

potential ϕ , from the lithium concentration c_2 , the Poisson equation is used:

$$\frac{d^2 \phi}{dx^2} = \frac{c_2 - c_{2eq}}{F_c \epsilon_0 \epsilon_r} \quad (10)$$

Where c_{2eq} is the equilibrium concentration of mobile lithium of LiPON. In order to solve the system of differential equations, the following boundary conditions are applied:

$$\frac{dc}{dt} = 0 \text{ for } x = 0 \quad (11)$$

$$\frac{dc}{dt} = -\frac{dc_2}{dt} = \frac{I_c}{AF_c} \text{ for } x = x_{LCO} \quad (12)$$

$$\phi = 0 \text{ for } x = x_{LCO} + x_{LiPON} \quad (13)$$

$$E = -\frac{d\phi}{dx} = \frac{q_c}{A_{elec} \epsilon_0 \epsilon_r} \text{ for } x = x_{LCO} \quad (14)$$

$$\frac{dc_2}{dt} = \frac{I_A}{AF_c} \text{ for } x = x_{LCO} + x_{LiPON} \quad (15)$$

$$E = -\frac{d\phi}{dx} = \frac{q_A}{A_{elec} \epsilon_0 \epsilon_r} \text{ for } x = x_{LCO} + x_{LiPON} \quad (16)$$

The charge accumulated on the anode and the cathode, q_A , q_C are the integral of the difference between the injected current I_{app} and the reaction current at each electrode

$$q_A = \int_0^T dt (I_{app} - I_A) \quad (17)$$

$$q_C = \int_0^T dt (I_{app} - I_C) \quad (18)$$

I_A and I_C , defined by the Butler-Volmer equation as:

$$I_C = i_{01c} c (1-c_2) \exp\left(\frac{\alpha F_c}{R_g T} \eta\right) - i_{02c} (1-c) c_2 \exp\left(-\frac{(1-\alpha) F_c}{R_g T} \eta\right) \quad (19)$$

And

$$I_A = i_{01a} c_2 \exp\left(\frac{\alpha F_c}{R_g T} \eta\right) - i_{02a} (1-c_2) \exp\left(-\frac{(1-\alpha) F_c}{R_g T} \eta\right) \quad (20)$$

The overpotential η is the potential drop between the two electrodes and is equal to the difference between the cathode voltage (ϕ_{LCO}) and the relaxation voltage (ϕ_{OCV})

$$\eta = \phi_{LCO} - \phi_{OCV} \quad (21)$$

In the case of the anode current I_A the lithium metal anode is considered ideal, i.e., the interface concentration of lithium inside the electrode and its activity are assumed to be constant and are not included into the equation, as in the cathode case. The presented model implements the constant current operation of the cell by imposing a fixed value of I_{app} . The current sign is positive during charge and negative during discharge. If a voltage ϕ_{app} is imposed, the corresponding current is calculated by an integral control which converts the potential different to a current by means of a constant R_s :

$$I_{app} = \int_0^T dt \frac{\phi_{app} - \phi_{LCO}}{R_s} \quad (22)$$

2.3. Model Parameters Extractions

We can now come back to the Equation 1 and develop it according to the theory.^[45] In particular, we can write the relation between the chemical potential and the equilibrium open circuit voltage (OCV) ϕ_{OCV} for the LCO cathode:

$$\phi_{OCV}(c) = -\frac{1}{q_0}(\tilde{\mu} - \tilde{\mu}_{anode}) = -\frac{1}{q_0}\tilde{\mu} \quad (23)$$

Where $\tilde{\mu}_{anode}$ is the OCV for the lithium anode, assumed to be constant and equal to 0V, according to the aforementioned hypothesis of ideal interface. We can re-write Equation 1 as:

$$\frac{\partial c}{\partial t} = -\frac{1}{\partial x} \left(M_{01} c_0 c (1-c) \frac{\partial c}{\partial x} \frac{\partial \tilde{\mu}}{\partial c} \right) = -\frac{1}{\partial x} \left(D \frac{\partial c}{\partial x} \right) \quad (24)$$

Where D , the diffusion coefficient, has been defined as:

$$D = M_{01} c_0 (1-c) \frac{\partial \tilde{\mu}}{\partial c} = -\frac{M_{01} c_0 (1-c)}{q_0} \frac{\partial \phi_{OCV}}{\partial c} \quad (25)$$

The model depends now on the two parameters $\phi_{OCV}(c)$ and M_{01} , and their dependence with respect to the intercalation fraction c ; both being experimentally measured by means of the galvanostatic-intermittent-titration technique (GITT).^[46–50] In the present work, GITT is performed on a 10 μm LCO device at 25°C. The temperature does not impact the LCO diffusion, due to the high activation energy (Figure S3, Supporting Information). Data has been treated as exposed in the methods section (Figures S5–S7, Supporting Information). The obtained OCV and diffusion coefficient D are shown in Figure 2c,d. An important feature of the OCV is the order–disorder transition at ≈ 0.5 ,^[51–54] which is exploited to set the half-intercalation point ($c=0.5$) of the material. The OCV and the diffusion coefficient extracted in the present work are both in good agreement with literature^[33,55–58] for (101)-(104) oriented LCO crystal.^[30] As show in Figure 2c,d, the low SOC state (high intercalation fraction) corresponds to the voltage plateau at 3.9 V and a very low diffusion coefficient. Following, the OCV starts rising and the diffusion coefficient, stabilizes around $5 \times 10^{-14} \text{ m}^2 \text{ s}^{-1}$ after a sharp increase. Concurrently with the voltage plateau, the LCO withstand a semiconductor-to-metal transition which determines a localization/delocalization of electrons cloud (Mott transition)^[59–63] altogether with a c axis stretching.^[51] This transition is pointed out to be the main cause of the diffusion coefficient variation^[54,62–65] and it is known that the capacity delivered in this region can be exploited only at minuscule current density. It is possible to divide the LCO into two regions with respect to state-of-charge (SOC): from 0 to 30% the LCO solid diffusion is very low, and the capacity can be exploited only at very low current. For SOC > 30% the diffusion coefficient is as high as $1 \times 10^{-13} \text{ m}^2 \text{ s}^{-1}$ and the capacity can be delivered even at high current density.

To conclude the model development, lithium mobility in LiPON^[50,66,67] and charge transfer coefficient are still missing. Electrochemical impedance spectroscopy (EIS) can provide the required information to complete the picture. In Figure 2b, an example of EIS data, altogether with the PDE based fitting, is reported (Figures S2 and S8, Supporting Information). The measurement setup is a two electrode test, and it is not possible to decouple the anode and cathode contributions. For this

reason, anode and cathode charge transfer currents are then assumed equal.

2.4. Model Results

The simulation results for lithium distribution in LCO are reported hereafter. Figure 2e depicts the discharge capacity as a function of the current rate, for a constant diffusion model and a variable diffusion model. The comparison between the variations of the delivered capacity for the two models shows how the variable diffusion is capable of simultaneously accounting for a large loss at low current and a good stability at high current density. The constant diffusion model, instead, can capture only one aspect at a time, depending on the chosen mobility. A comparison between constant and variable diffusion coefficient simulations is proposed also for predicting lithium concentration inside the LCO upon charge and discharge process (Figure 2f). Concerning the constant voltage (CV) charge at 4.2 V, the effect of the variable diffusion is a charge carrier accumulation in the bulk for high intercalation fractions. Overall, both show a proper final profile and a homogeneous charging profile. During constant current (CC) discharge with constant diffusion, the accumulation at the interface is constant during the whole process and increases with increasing current rate. Furthermore, the variable diffusion coefficient confers a peculiar shape to the lithium concentration profile: the discharge proceeds smoothly until the low diffusion coefficient region and then, an abrupt increase determines the end of the discharge. The delivered capacity, after the abrupt loss at very low current rate, stabilizes $\approx 40\%$ – 50% of the charged capacity, thus resulting in the capacity asymptote observed in Figure 2e.

2.5. Discharge Capacity Variation with Thickness and Current Density, and Model Validation

Figure 3a,b shows the CV charge and CC discharge curve fitting. The model and measurements account for a first charge with a theoretical ($x = 0.5$) capacity of 685 mA h cm^{-3} for all four considered thicknesses. The discharge for all four stacks present the characteristic loss of 30% capacity both in the measured and simulated curves. In Figure 3c-f, the charge/discharge behavior, over 10 cycles of the four realized stacks (5, 10, 20, and 30 μm LCO cells), is presented. The result substantiates that the capacity loss is limited to the first cycle and all subsequent charge-discharge are performed at $\approx 100\%$ coulombic efficiency (ratio between discharge capacity and charge capacity near 1). The results not only validate the model with the use of a variable diffusion coefficient, but also provide an excellent demonstration of the cycling possibility of thick LCO cathode. The most important feature remains that the model is capable of explaining the 30% capacity loss exhibited during the first cycle. Particularly, this loss is associated with the low diffusion coefficient at low SOC measured in the previous section. The loss is intrinsic to the LCO material and independent of cathode thickness, electrolyte (liquid or solid) or anode (lithium-metal or lithium-free) configuration (Figure S1, Supporting Information). We would expect a proper cycling capability at high thickness

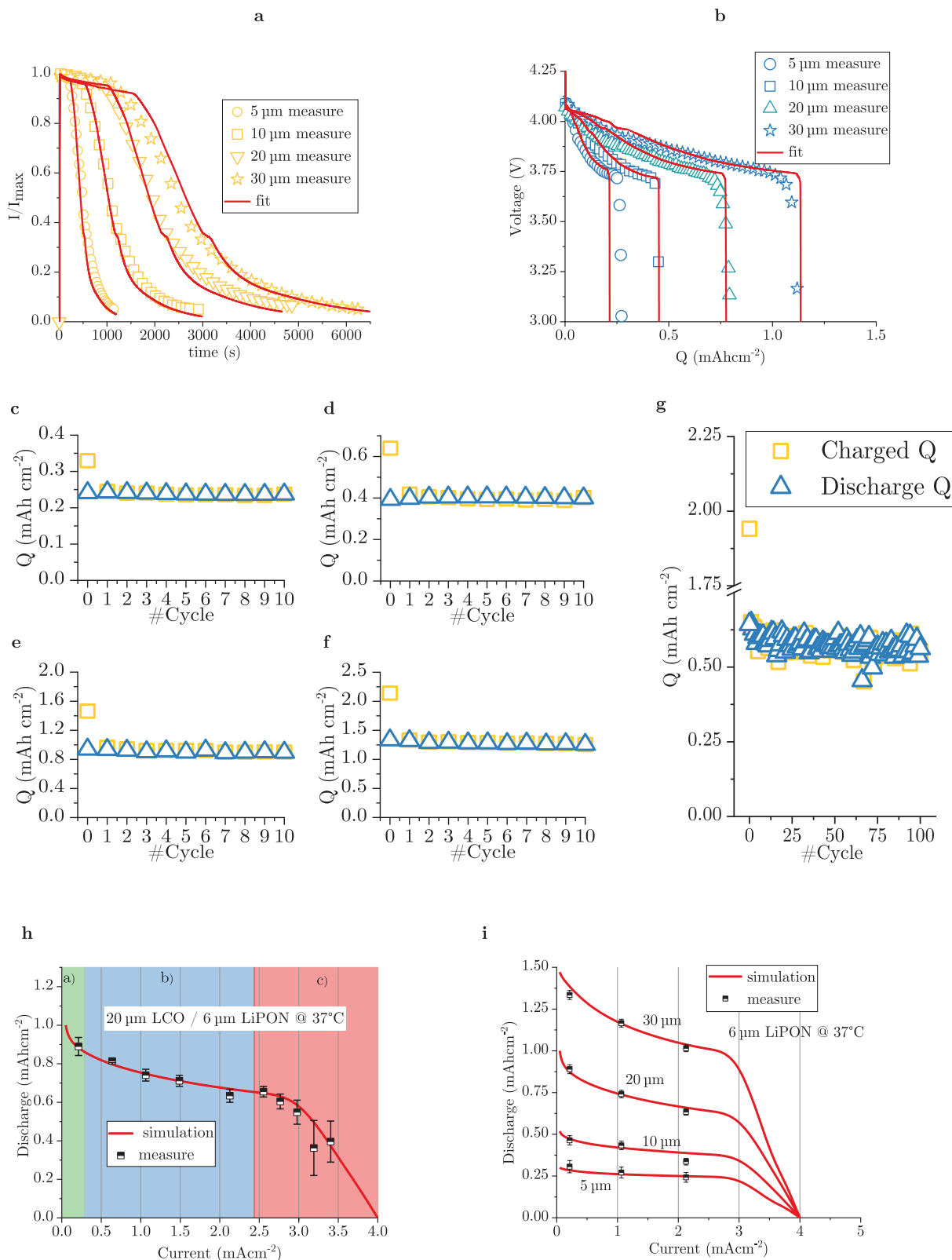


Figure 3. Experimental results and model validation. a,b) Simulated and measured CV charge (CV @ 4.3V down to $1 \times 10^{-2} \text{ mA cm}^{-2}$) and CC discharge (CC @ 1 mA cm^{-2} down to 3 V) curve for 5, 10, 20, and 30 μm thick LCO at 37 °C. c–f) Capacity delivered versus cycle number at 100% DOD (same protocol as (a) and (b)) for 5, 10, 20, and 30 μm thick LCO. Capacity loss (–30%) between first charge and first discharge is observed for all thicknesses. g) Cycling results for 30 μm thick LCO at 60% DOD. h) Simulated (in red) and measured (black points) delivered capacity as a function of the current density for 20 μm thick LCO cathode at 37 °C. i) Simulated and measured delivered capacity as a function of the current density: comparison between 5, 10, 20, 30 μm thick LCO at 37 °C.

and no additional loss of capacity during the first cycle: the loss is actually proportional to the initial charge hence, the available capacity is predicted to increase linearly with increasing LCO thickness. In addition, in order to demonstrate a good cycle life, in Figure 3g, the cycling at 60% depth-of-discharge (DOD) of a 30 μm battery is reported for 100 cycles. To the best of our knowledge, this is the highest recorded performance, in terms of delivered capacity and cycling stability, for a 30 μm thick cathode in an all-solid-state lithium free configuration reported so far. Figure 3h depicts the delivered capacity versus current density for a 20 μm thick LCO cathode and 6 μm thick LiPON electrolyte cell at 37 $^{\circ}\text{C}$. Figure 3i shows the simulation vs measurement comparison extended to all tested cathode thicknesses. The agreement between the model and the measurements is optimal (mean error between measurement and simulation $\approx 2\%$ over the total capacity, between 0 and 3 mA cm^{-2}) and the measurements show a small standard deviation (4%). At higher current density, the increase in measurement standard deviation (up to 40%) can be attributed to the amplification effect on the uncertainty of internal resistance, near the voltage plateau (Figure S4, Supporting Information). From the presented results, it is possible to split the device behavior in three operating regimes:

1. The first region (green in Figure 3c) corresponds to a fast decrease in the available capacity with increasing current density. We can correlate this first behavior to the effect of the small diffusion coefficient between 0 and 30% SOC.
2. The second region (blue in Figure 3c) highlights a steady decrease in the available capacity, which resemble the behavior of the constant diffusion case, as previously shown in Figure 2e. This behavior is consistent with an almost constant diffusion coefficient at low intercalation fraction. The slope is cathode thickness-dependent, as clearly shown in Figure 3g. This dependence can be easily understood, recalling once again Figure 2. In particular, Figure 2f (in the case of constant diffusion discharge at high current) presents a typical

concentration profile, as we may expect inside the LCO. We can then observe that the 10 micrometers near the LiPON are far more discharged than the 10 micrometers closer to the current collector. We deduce that, at iso-current, the 10 μm stack will deliver, in proportion, more capacity than the 30 μm , hence the different slopes in Figure 3i.

3. In the third region (red in Figure 3c), a new phenomenon takes place: the ohmic drop. Up to this point, we disregarded the effect of the internal resistance on the delivered capacity, due to its minor impact with respect to the diffusion limitation in LCO. In particular, the ohmic drop results in a shift of the discharge curve towards lower potential (Figure S4, Supporting Information). At low current density, this shift has minor impact due to the particular shape of the discharge curve between 4.2 and 3 V. As soon as the shift approached 900 mV, the voltage plateau of LCO approaches the 3 V cut-off potential. From this point on, a fast capacity loss is observed down to zero delivered capacity above 3 V. The transition is quite fast, due to the LCO voltage profile flatness. In order to improve this part, the electrolyte resistance has to be decreased, by means of thinner layer or the selection of a material with a higher ionic conductivity.

3. Discussion

Figure 4a reports a comparison for all-solid-state thin-film batteries between the results of current work and other studies reported in literature. Most of the literature results are in line with our model prediction. At the same time, Figure 4a clearly highlights the superior performance of the present work for the considered current density range. After validating our 1D model using experimental data, it is possible to push the simulation results forward and consider higher cathode thickness, in order to estimate both the maximum capacity and power, deliverable for an optimal cell design. In Figure 4b, we report the evolution

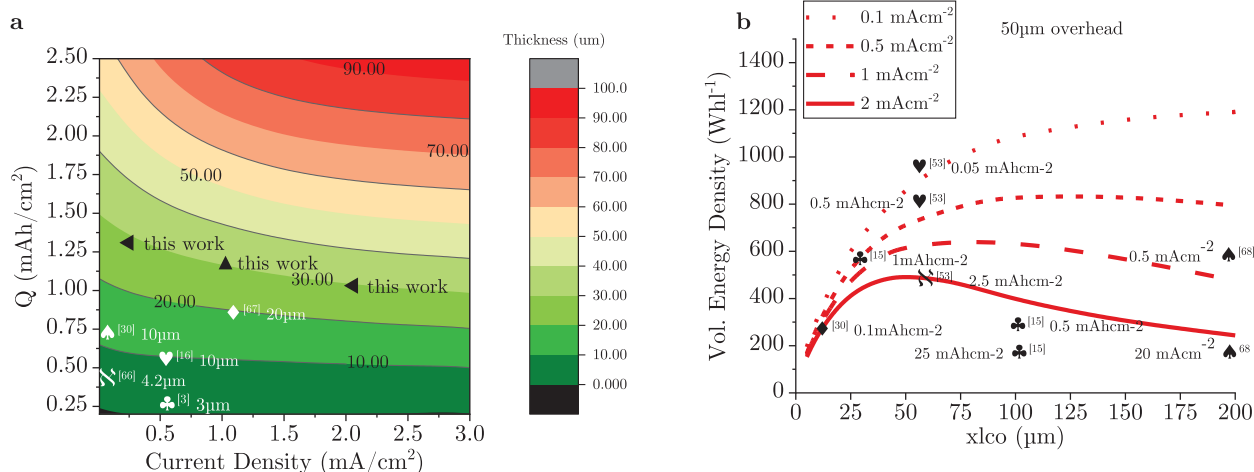


Figure 4. Model prediction and state-of-art comparison. a) Model prediction up to 100 μm thick LCO with main literature results;^[3,16,32,75,76] this work presents the highest areal capacity among all-solid state, 100%-active anode-free batteries. b) Volumetric energy density comparison between all available LCO based battery technologies (thin-film, composite all solid-state and slurry). The total volume is calculated assuming 50 μm of overhead on top of the cathode and the energy density assuming 4 V of average discharge potential for all references.^[15,32,55,68]

of the delivered volumetric energy according to the simulation results (in red), at different current densities. In order to estimate the volume of the device as a whole, we added 50 μm of non-active material (overhead) assuming an average voltage of 4 V during the discharge. It is observed that the relation between the cathode thickness and the volumetric energy density varies with applied current (no expected gain above 100 and 50 μm thick LCO for 0.5 and 2 mA cm^{-2} , respectively). In the same figure, a comparison between different technologies reported in literature is proposed. In particular, the classic slurry electrode^[55] shows comparable performance with respect to thin-film at moderate electrode thickness (50 μm). Porous electrode^[68], in contrast, shows even better performance than thin-film batteries at extremely high current density (20 mA cm^{-2}) and thicknesses (200 μm) thanks to high conductive liquid electrolyte percolation, at the cost of a reduction in capacity at lower current rating. 100 μm LCO/carbon-nanofibers (CNFs)^[15] structure shows the potentiality of this solution in order to keep a constant energy density for almost two decades of current densities; the cost is a drastic reduction of the volumetric energy density linked with the void between CNFs, as observed in the porous-electrode design. The reported thin-film battery examples^[15,32] are, on the other hand, aligned with the model predictions. Hence, an optimal design will reach unexpected capacity density, at high current, with respect to results reported in literature for all-solid-state batteries. Notwithstanding, the limitation introduced by the drop in the diffusion coefficient is expected to be still present. In order to further enhance the performance, it would be necessary to act at the cathode material level. This additional boost is possible through LCO doping, which results in a suppression of the semiconductor-to-metal transition and a parallel increase in diffusion coefficient. The different solutions proposed so far seems to be successful, at the expense of a slight decrease in the available capacity.^[69–73] While, optimizations of the electrode design and/or at the material level are limited by the available technologies, an additional degree of freedom is enabled through the charge–discharge protocol optimization, in particular by considering a cascaded discharge approach.^[74]

4. Experimental Section

Precession Electron Diffraction Measurement: PED patterns for the analysis of LCO crystal orientation were obtained using a JEOL 2010 FEG TEM equipped with a NanoMegas ASTAR. All patterns were obtained using a precession angle of 0.96°.

Scanning Electron Microscopy: LCO crystal structure observation by means of secondary electron scanning electron microscopy were carried out on a Hitachi S-5500 SEM equipment. SEM samples were manually cut by means of a diamond scribe pen.

Scanning Micro-Raman Spectroscopy: Chemical analysis by means of scanning Raman spectroscopy were carried out on a Renishaw InVia Reflex micro-Raman spectrometer equipped with a 100X (N.A. 0.85) LEICA objective. The laser source was a 532 nm Renishaw RL532C100 laser with a power of 10 μW . Samples were manually cut by means of a diamond scribe pen. Therefore, the LCO surface was not perfectly flat, and even if an optimal zone is chosen by mean of optical observation, a certain topography is expected on the analyzed surface.

Scanning Micro-Raman Spectroscopy Data Processing: Raman spectra were corrected by fitting the baseline with a linear function

and subtracting it to the signal (Figure S10, Supporting Information). Then the measured data were fitted by a sum of Laurentian functions as explained in details in Supporting Information (Figures S11 and S12, Supporting Information).

Electrochemical Measurements: All electrochemical measurements were performed on a Biologic VMP3 Multichannel Potentiostat. The measurements were carried out in a Cascade SUMMIT200 Probe Station in dry air environment. Impedance spectroscopy measurement was performed between 1 MHz and 100 mHz. The cell was stimulated with a 10 mV sinusoidal voltage and the current response was measured. Each measurement was averaged 5 times for each frequency. Charge protocol was a Constant Potential (CV) stimulation of the cell at 4.3 V. The current was monitored and the charge stopped when 5% of the initial current was reached. Discharge protocol was a Constant Current (CC) stimulation. The discharge was stopped when the cell potential reaches 3 V.

Galvanostatic Intermittent Titration Technique (GITT): GITT measurement was performed using a Biologic VMP3 Multichannel Potentiostat under argon atmosphere (Figure S5, Supporting Information).

Galvanostatic Intermittent Titration Technique (GITT) Data Processing: GITT measurement data are treated as reported in Supporting Information (Figures S6 and S7, Supporting Information).

PDE Simulation: The physical model was solved by means of finite element methods in COMSOL multiphysics. All equations are implemented by means of the Weak Form PDE interface.

Conflict of Interest

The authors declare no conflict of interest.

Data Availability Statement

The data that support the findings of this study are available from the corresponding author upon reasonable request.

Supporting Information

Supporting Information is available from the Wiley Online Library or from the author.

Keywords

high-capacity, LCO, lithium-free, rate-capability, solid-state, thick-cathodes, thin-films

Received: December 7, 2022
Published online:

- [1] Y. Li, M. Zhu, V. K. Bandari, D. D. Karnaushenko, D. Karnaushenko, F. Zhu, O. G. Schmidt, *Adv. Energy Mater.* **2022**, *12*, 2103641.
- [2] K. Yoon, S. Lee, K. Oh, K. Kang, *Adv. Mater.* **2022**, *34*, 2104666.
- [3] A. Suzuki, S. Sasaki, T. Jimbo, *J. Phys.: Conf. Ser.* **2019**, *1407*, 012037.
- [4] C. Sun, J. Liu, Y. Gong, D. P. Wilkinson, J. Zhang, *Nano Energy* **2017**, *33*, 363.
- [5] C. Li, Z.-y. Wang, Z.-j. He, Y.-j. Li, J. Mao, K.-h. Dai, C. Yan, J.-c. Zheng, *Sustainable Mater. Technol.* **2021**, *29*, e00297.
- [6] T. Shi, Q. Tu, Y. Tian, Y. Xiao, L. J. Miara, O. Kononova, G. Ceder, *Adv. Energy Mater.* **2020**, *10*, 1902881.

- [7] J. Wu, Z. Ju, X. Zhang, X. Xu, K. J. Takeuchi, A. C. Marschilok, E. S. Takeuchi, G. Yu, *ACS Nano* **2022**, *16*, 4805.
- [8] H. Kim, S. K. Oh, J. Lee, S. W. Doo, Y. Kim, K. T. Lee, *Electrochim. Acta* **2021**, *370*, 137743.
- [9] Y. Kuang, C. Chen, D. Kirsch, L. Hu, *Adv. Energy Mater.* **2019**, *9*, 1901457.
- [10] J. Newman, W. Tiedemann, *AIChE J.* **1975**, *21*, 25.
- [11] T. R. Ferguson, M. Z. Bazant, *J. Electrochem. Soc.* **2012**, *159*, A1967.
- [12] W. Lai, F. Ciucci, *Electrochim. Acta* **2011**, *56*, 4369.
- [13] J. Y. Kim, J. Park, M. J. Lee, S. H. Kang, D. O. Shin, J. Oh, J. Kim, K. M. Kim, Y.-G. Lee, Y. M. Lee, *ACS Energy Lett.* **2020**, *5*, 2995.
- [14] M. Li, T. Liu, Z. Shi, W. Xue, Y. Hu, H. Li, X. Huang, J. Li, L. Suo, L. Chen, *Adv. Mater.* **2021**, *33*, 2008723.
- [15] H. Zhang, H. Ning, J. Busbee, Z. Shen, C. Kiggins, Y. Hua, J. Eaves, J. Davis, T. Shi, Y. T. Shao, J. M. Zuo, X. Hong, Y. Chan, S. Wang, P. Wang, P. Sun, S. Xu, J. Liu, P. V. Braun, *Sci. Adv.* **2017**, *3*, 2.
- [16] A. C. Johnson, A. J. Dunlop, R. R. Kohlmeier, C. T. Kiggins, A. J. Blake, S. V. Singh, E. M. Beale, B. Zahiri, A. Patra, X. Yue, J. B. Cook, P. V. Braun, J. H. Pikul, *J. Power Sources* **2022**, *532*, 231359.
- [17] J. Y. Kim, S. Jung, S. H. Kang, M. J. Lee, D. Jin, D. O. Shin, Y.-G. Lee, Y. M. Lee, *J. Power Sources* **2022**, *518*, 230736.
- [18] M. J. Wang, E. Carmona, A. Gupta, P. Albertus, J. Sakamoto, *Nat. Commun.* **2020**, *11*, 5201.
- [19] C.-J. Huang, B. Thirumalraj, H.-C. Tao, K. N. Shitaw, H. Sutiono, T. T. Hagos, T. T. Beyene, L.-M. Kuo, C.-C. Wang, S.-H. Wu, W.-N. Su, B. J. Hwang, *Nat. Commun.* **2021**, *12*, 1452.
- [20] A. J. Louli, M. Coon, M. Genovese, J. deGooyer, A. Eldesoky, J. R. Dahn, *J. Electrochem. Soc.* **2021**, *168*, 020515.
- [21] H. Pan, T. Fu, G. Zan, R. Chen, C. Yao, Q. Li, P. Pianetta, K. Zhang, Y. Liu, X. Yu, H. Li, *Nano Lett.* **2021**, *21*, 5254.
- [22] F. Sagane, K.-i. Ikeda, K. Okita, H. Sano, H. Sakaebe, Y. Iriyama, *J. Power Sources* **2013**, *233*, 34.
- [23] K. Mizushima, P. Jones, P. Wiseman, J. Goodenough, *Mater. Res. Bull.* **1980**, *15*, 783.
- [24] D. Danilov, R. A. H. Niessen, P. H. L. Notten, *J. Electrochem. Soc.* **2011**, *158*, A215.
- [25] N. Kazemi, D. L. Danilov, L. Haverkate, N. J. Dudney, S. Unnikrishnan, P. H. Notten, *Solid State Ionics* **2019**, *334*, 111.
- [26] L. Raijmakers, D. Danilov, R.-A. Eichel, P. Notten, *Electrochim. Acta* **2020**, *330*, 135147.
- [27] L. Cabras, V. Oancea, A. Salvadori, *arXiv:2104.05424 [cond-mat]* **2021**, arXiv: 2104.05424.
- [28] Y. Matsuda, N. Kuwata, J. Kawamura, *Solid State Ionics* **2018**, *320*, 38.
- [29] S. Oukassi, R. Salot, A. Bazin, C. Secouard, I. Chevalier, S. Poncet, S. Poulet, J.-M. Boissel, F. Geffraye, J. Brun, in *2019 IEEE International Electron Devices Meeting (IEDM)*, IEEE, San Francisco, CA, USA **2019**, pp. 26.1.1–26.1.4.
- [30] J. B. Bates, N. J. Dudney, B. J. Neudecker, F. X. Hart, H. P. Jun, S. A. Hackney, *J. Electrochem. Soc.* **2000**, *147*, 59.
- [31] Julien, Mauger, Hussain, *Materials* **2019**, *12*, 2687.
- [32] J. Trask, A. Anapolsky, B. Cardozo, E. Januar, K. Kumar, M. Miller, R. Brown, R. Bhardwaj, *J. Power Sources* **2017**, *350*, 56.
- [33] J. Xie, N. Imanishi, T. Matsumura, A. Hirano, Y. Takeda, O. Yamamoto, *Solid State Ionics* **2008**, *179*, 362.
- [34] S. Shiraki, Y. Takagi, R. Shimizu, T. Suzuki, M. Haruta, Y. Sato, Y. Ikuhara, T. Hitosugi, *Thin Solid Films* **2016**, *600*, 175.
- [35] G. Hasegawa, N. Kuwata, Y. Tanaka, T. Miyazaki, N. Ishigaki, K. Takada, J. Kawamura, *Phys. Chem. Chem. Phys.* **2021**, *23*, 2438.
- [36] P. J. Bouwman, B. A. Boukamp, H. J. M. Bouwmeester, P. H. L. Notten, *J. Electrochem. Soc.* **2002**, *149*, A699.
- [37] S. Tintignac, R. Baddour-Hadjean, J.-P. Pereira-Ramos, R. Salot, *Electrochim. Acta* **2012**, *60*, 121.
- [38] C. M. Julien, A. Mauger, *AIMS Mater. Sci.* **2018**, *5*, 650.
- [39] Y. Matsuda, N. Kuwata, T. Okawa, A. Dorai, O. Kamishima, J. Kawamura, *Solid State Ionics* **2019**, *335*, 7.
- [40] L. Le Van-Jodin, D. Rouchon, V. Le, I. Chevalier, J. Brun, C. Secouard, *J. Raman Spectrosc.* **2019**, *50*, 1594.
- [41] I. Minoru, I. Yasutoshi, O. Zempachi, T. Yasufumi, T. Akimasa, *J. Raman Spectrosc.* **1997**, *28*, 5.
- [42] E. Flores, P. Novák, E. J. Berg, *Front. Energy Res.* **2018**, *6*, 82.
- [43] G. Frenning, M. Strømme, *J. Appl. Phys.* **2001**, *90*, 5570.
- [44] R. E. White, J. O. Bockris, B. E. Conway, (Eds), *Modern Aspects of Electrochemistry*, Springer US, Boston, MA **1983**.
- [45] W. McKinnon, Ph.D. thesis, University of British Columbia, **1980**.
- [46] C. J. Wen, B. A. Boukamp, R. A. Huggins, W. Weppner, *J. Electrochem. Soc.* **1979**, *126*, 2258.
- [47] W. Weppner, R. A. Huggins, *J. Electrochem. Soc.* **1977**, *124*, 1569.
- [48] I. O. Santos-Mendoza, J. Vázquez-Arenas, I. González, G. Ramos-Sánchez, C. O. Castillo-Araiza, *Int. J. Chem. React. Eng.* **2019**, *17*, 6.
- [49] A. Nickol, T. Schied, C. Heubner, M. Schneider, A. Michaelis, M. Bobeth, G. Cuniberti, *J. Electrochem. Soc.* **2020**, *167*, 090546.
- [50] A. Rudy, A. Mironenko, V. Naumov, A. Novozhilova, A. Skundin, I. Fedorov, *Batteries* **2021**, *7*, 21.
- [51] J. N. Reimers, J. R. Dahn, *J. Electrochem. Soc.* **1992**, *139*, 2091.
- [52] A. Van der Ven, M. K. Aydinol, G. Ceder, G. Kresse, J. Hafner, *Phys. Rev. B* **1998**, *58*, 2975.
- [53] W. McKinnon, J. Dahn, *Solid State Commun.* **1983**, *48*, 43.
- [54] A. Van der Ven, M. K. Aydinol, G. Ceder, *J. Electrochem. Soc.* **1998**, *145*, 2149.
- [55] J. Choi, B. Son, M.-H. Ryou, S. H. Kim, J. M. Ko, Y. M. Lee, *J. Electrochem. Sci. Technol.* **2013**, *4*, 27.
- [56] Z. Li, F. Du, X. Bie, D. Zhang, Y. Cai, X. Cui, C. Wang, G. Chen, Y. Wei, *J. Phys. Chem. C* **2010**, *114*, 22751.
- [57] H. Xia, L. Lu, G. Ceder, *J. Power Sources* **2006**, *159*, 1422.
- [58] Y.-I. Jang, B. J. Neudecker, N. J. Dudney, *Electrochem. Solid-State Lett.* **2001**, *4*, A74.
- [59] N. F. Mott, *Rev. Mod. Phys.* **1968**, *40*, 677.
- [60] C. A. Marianetti, G. Kotliar, G. Ceder, *Nat. Mater.* **2004**, *3*, 627.
- [61] E. Flores, N. Mozhzhukhina, U. Aschauer, E. J. Berg, *ACS Appl. Mater. Interfaces* **2021**, *13*, 22540.
- [62] M. Ménétrier, I. Saadoun, S. Levasseur, C. Delmas, *J. Mater. Chem.* **1999**, *9*, 1135.
- [63] F. Xiong, H. J. Yan, Y. Chen, B. Xu, J. X. Le, C. Y. Ouyang, *Int. J. Electrochem. Sci.* **2012**, *7*, 11.
- [64] N. Nadkarni, T. Zhou, D. Fraggedakis, T. Gao, M. Z. Bazant, *Adv. Funct. Mater.* **2019**, *29*, 1902821.
- [65] H. Zhou, F. Xin, B. Pei, M. S. Whittingham, *ACS Energy Lett.* **2019**, *4*, 1902.
- [66] Y. Hamon, A. Douard, F. Sabary, C. Marcel, P. Vinatier, B. Pecquenard, A. Levasseur, *Solid State Ionics* **2006**, *177*, 257.
- [67] L. Le Van-Jodin, F. Ducroquet, F. Sabary, I. Chevalier, *Solid State Ionics* **2013**, *253*, 151.
- [68] R. He, G. Tian, S. Li, Z. Han, W. Zhong, S. Cheng, J. Xie, *Nano Lett.* **2022**, *22*, 2429.
- [69] S. Myung, *Solid State Ionics* **2001**, *139*, 47.
- [70] J. H. Song, A. Kapylou, H. S. Choi, B. Y. Yu, E. Matulevich, S. H. Kang, *J. Power Sources* **2016**, *313*, 65.
- [71] Y. Xu, X. Wang, Z. Wang, S. Wang, X. Zhu, D. Li, J. Yu, *Nanoscale* **2020**, *12*, 10205.
- [72] Q. Liu, X. Su, D. Lei, Y. Qin, J. Wen, F. Guo, Y. A. Wu, Y. Rong, R. Kou, X. Xiao, F. Aguesse, J. Bareño, Y. Ren, W. Lu, Y. Li, *Nat. Energy* **2018**, *3*, 936.
- [73] L. Sun, Z. Zhang, X. Hu, H. Tian, Y. Zhang, X. Yang, *J. Electrochem. Soc.* **2019**, *166*, A1793.
- [74] G. Depresse, C. Secouard, S. Oukassi, Assembly of electrical energy storage or production cells comprising a management circuit for managing the cells, *US Patent 17/228,557*.
- [75] N. Dudney, *Mater. Sci. Eng., B* **2005**, *116*, 245.
- [76] T. Jimbo, S. Sasaki, A. Suzuki, I. Kimura, K. Suu, *ECS Meet. Abstr.* **2013**, MA2013-02, 1235.